IAEA nuclear fusion

Geometric dependencies of the mean $E \times B$ shearing rate in negative triangularity tokamaks

To cite this article before publication: Rameswar Singh *et al* 2023 *Nucl. Fusion* in press https://doi.org/10.1088/1741-4326/ad0605

Geometric dependencies of the mean $E \times B$ shearing rate in negative triangularity tokamaks

Rameswar Singh and P H Diamond

Department of Astronomy and Astrophysics, University of California San Diego, 9500 Gilman Dr, La Jolla, CA 92093, United States of America

E-mail: `rsingh@ucsd.edu`

A O Nelson

Columbia University, New York, NY 10027, USA

Abstract. This paper presents a comparative study of the poloidal distribution of mean $E \times B$ shearing rate for positive triangularity (PT) and negative triangularity (NT) tokamaks. The effects of flux surface up-down asymmetry due to asymmetric upper and lower triangularities is also considered. Both direct eddy straining and effects on Shafranov shift feedback loops are examined. Shafranov shift increases the shearing rate at all poloidal angles for all triangularities, due to flux surface compression. The maximum shearing rate bifurcates at a critical triangularity $\delta_{crit}(\lesssim 0)$. Thus, the shearing rate is maximal *off* the outboard mid-plane for NT, while it is maximal *on* the outboard mid-plane for PT. For up-down asymmetric triangularity, the usual up-down symmetry of the shearing rate is broken. The shearing rate at the out board mid-plane is lower for NT than for PT suggesting that the shearing efficiency in NT is reduced. Implications for turbulence stabilization and confinement improvement in high-β_p NT and ITB discharges are discussed.

1. Introduction

Negative triangularity (NT) discharges have demonstrated H-mode-like pressure and energy confinement times for L-mode-like edge conditions [1–5]. Improved confinement with an L-mode edge is advantageous to a fusion reactor [6, 7]. This is because NT L-mode is an attractive operation regime that is naturally free of ELMs. Also, NT discharges manifest very weak degradation of confinement with power [1], along with broader scrape off layer (SOL) heat flux widths as compared to conventional PT H-mode cases, reduced fluctuation levels [1–4], and reduced plasma wall interaction [8]. However, understanding of the physics of confinement improvement and L-H transition in NT is still in it's infancy. Improved confinement in L-mode should facilitate easy access to H-mode i.e., with lesser power than the conventional L-H transition threshold. While this is observed at weak negative triangularities, H-mode becomes completely inaccessible at strong negative triangularities($\delta_u < -0.18$) even if high power is applied. This has been linked to loss of access to 2nd stability region of the infinite-n ideal ballooning modes [9, 10]. This model is built upon a previous study predicting reduced pedestal height, clamped by degraded PB and KBM stability, due to closed access to the second stability region for ballooning modes in the case of negative triangularity [11]. Some of the past experiences with conventional H-mode discharges suggest that 2nd stability access may not be a necessary requirement for H mode. Loss of 2nd stability, triggered by changing the squareness of plasma shape, only changes low frequency high amplitude ELMs to high frequency low amplitude ELMs, without eliminating the H-mode [12, 13]. A recent experimental study using ECE-imaging suggests that NT edge pressure is limited by low-n interchange type MHD modes or resistive ballooning modes [14]. Gyrokinetic simulations [3, 4, 15–19] attribute linear stabilization of trapped electron mode (TEM) or ion temperature gradient (ITG) mode to the observed reduction of turbulence and transport in the core of NT configuration. One thus naturally wonders about the role of mean ExB shear in NT confinement and L-H transition physics. Clearly, the ideas in the NT landscape are still evolving, and a consensus on confinement and L-H physics is still lacking. This begs for a study of the mechanisms of turbulence saturation and transport in NT shapes.

Zonal flow shear [20–22] and mean ExB shear are candidate players in the saturation of drift wave turbulence in tokamaks, and also play significant roles in the L-H transition. Both zonal flow shear and mean ExB shear break up turbulent eddies, thus reducing the turbulence coherence length [23]. As a result, transport is reduced, and regulated by both zonal flow and mean ExB shear. Our recent work shows that the zonal flows are weaker in NT than that in PT due to enhanced neoclassical polarization, from an increase in trapped fraction in NT [24]. As zonal flow lowers the threshold power for L-H transition [25], the prediction of reduced zonal flows in NT is consistent with the observation of increased power threshold for L-H transition. Note that no validated first principle theory of L-H transition [26,27] exists. However, the transition is almost always linked to transport bifurcation due to mean ExB shearing [25, 28, 29]. Similarly, core transport barriers in high poloidal beta reversed shear discharges - often called internal transport barriers (ITBs) - are sometimes linked to transport bifurcation induced by the local mean $E \times B$ shear [30–32].

Thus, $E \times B$ shear suppression of turbulence and transport is one of the key element of the physics of transport barriers. Given the significant role of mean $E \times B$ shear in transport barriers formation one wonders *what happens to the shearing rate when the flux surface shapes changes from the PT to NT?* This is precisely the aim of this paper, which illustrates magnetic geometry dependent features of the mean $E \times B$ shearing rate contrasting the effects of positive and negative triangularities. It is well known that magnetic geometry plays a role in shearing physics [33]. Here, we focus on the interplay of NT configuration with mean $E \times B$ shearing. Usually, shearing is considered as a flux surface averaged quantity. Experiments usually report the shearing rate at the outboard mid-plane. Here, we study *the poloidal structure of the mean $E \times B$ shearing rate as the flux surface shapes vary from PT to NT*, using Miller's parametrized equilibrium model [34]. This also allows the study of the local parametric dependence of the shearing rate with triangularity gradient, elongation, elongation gradient squareness, squareness gradient and Shafranov shift gradient as the triangularity changes from PT to NT. The significance of each of these shaping parameters are explained in table(1). All these local shaping parameters affect the shearing in a non-trivial way. We determine that the mean $E \times B$ shear at the out board mid-plane is lower for NT than that for PT. The maximal mean shear bifurcates at a critical triangularity $\delta_{crit} \lesssim 0$ and the shear is maximal off the mid-plane for NT. The shearing becomes up-down asymmetric for asymmetric flux surfaces owing to different upper and lower triangularities. Triangularity gradient reduces the shearing rate, while elongation and elongation gradient increases the mean shear. Negative squareness eliminates the geometric bifurcation for NT, and narrows the poloidal distribution of the shearing. As a result the flux surface averaged shearing rate becomes lower for negative squareness than that for positive squareness. ITB formation in high poloidal beta (β_p) discharges is frequently linked to transport bifurcation due to turbulence stabilization due to drift reduction/reversal by large Shafranov shift [35–37]. This interpretaion ignores the coupling of mean shear to Shafranov shift effects. Mean $E \times B$ shear exists in these discharges, after all. So, one wonders what happens to mean shear in high Shafranov shift regime? Our analysis shows that *the mean $E \times B$ shear increases with increasing Shafranov shift gradient, because of enhanced flux surface compression*. Thus, there is a direct boost of mean shear by the Shafranov shift, which complements the conventionally invoked Shafranov shift effect. This observation and the related physics analysis are the major results of this paper.

Shaping parameters	related to
Triangularity δ	how triangular the shape is
Triangularity gradient S_δ	radial variation of triangularity
Shafranov shift gradient R_0'	radial varition of shift of magnetic axis from geometric axis
Elongation κ	how elongated the shape is
Elongation gradient S_κ	radial variation of elongation
Squareness σ	how square the shape is
Squareness gradient S_σ	radial variation of squareness

Table 1. Shaping parameters and their meanings.

The rest of the paper is organized as follows. The dependencies of the shearing rate on different geometric parameters is calculated in Section 2. The results are discussed and conclusions are given in Section 3.

2. Flux surface geometry dependence of mean ExB shearing rate

The Hahm-Burrell formula for the mean $E\times B$ shearing rate [33], ignoring mean parallel flow shear, is obtained from a 2-point correlation calculation for an axisymmetric toroidal system and reads as

$$\omega_s = \left(\frac{\Delta\psi_0}{\Delta\zeta}\right)\frac{\partial^2}{\partial\psi^2}\Phi_0(\psi), \tag{1}$$

where $\Delta\psi_0$ is the turbulence correlation width in poloidal magnetic flux ψ and $\Delta\zeta$ is toroidal correlation angle of the ambient fluctuations. In fact, ψ is stream function for poloidal magnetic field and is poloidal magnetic flux (divided by 2π). The mean electrostatic potential is assumed to be a flux function i.e., $\Phi_0 = \Phi_0(\psi)$. Since, fluctuation diagnostics (such as Beam emission spectroscopy, Doppler back scattering etc.,) measure correlation length Δr in the radial co-ordinate r, it is useful to express $\Delta\psi$ in terms of Δr as $\Delta\psi = \Delta r\frac{\partial\psi}{\partial r}$. Here R is the major radius and B_θ is the poloidal magnetic field. Similarly, the toroidal correlation angle $\Delta\zeta$ can be expressed in terms of poloidal correlation angle $\Delta\theta$ as $\Delta\zeta = \nu\Delta\theta$, where $\nu = \frac{\vec{B}\cdot\vec{\nabla}\zeta}{\vec{B}\cdot\vec{\nabla}\theta} = \frac{I\mathcal{J}}{R^2\psi'}$ is the local safety factor. $I \equiv \frac{\mu_0}{2\pi}I^d_{pol}$ is an effective measure of the total poloidal current I^d_{pol} (both plasma and toroidal field coil currents) outside the flux surface $\psi = const.$ $\mathcal{J}$ is the Jacobian of transformation from toroidal coordinates to orthonormal Euclidean coordinates, $\vec{r}(r,\theta,\zeta)$ with $\vec{r} = R\sin\zeta\hat{x} + R\cos\zeta\hat{y} + Z\hat{z}$ being the position vector in the euclidean space spanned by the unit basis vectors $(\hat{x},\hat{y},\hat{z})$. Notice that, $\mathcal{J}/\psi'$ is the Jacobian of the flux coordinates (ψ,θ,ζ). Therefore,

$$\frac{\Delta\psi_0}{\Delta\zeta} = \frac{\Delta r}{\Delta\theta}\frac{R^2\psi'^2}{I\mathcal{J}}, \tag{2}$$

where

$$\psi' = \frac{I(\psi)}{2\pi q(\psi)}\oint d\theta\frac{\mathcal{J}}{R^2}, \tag{3}$$

which has been obtained from the definition of the global safety factor q. Thus, *the magnetic geometry/topology dependence of the mean $E\times B$ shearing rate enters through the Jacobian $\mathcal{J}$, the major radius R and the radial gradient of poloidal flux i.e., ψ' for fixed $\frac{\partial^2}{\partial\psi^2}\Phi_0(\psi)$*. Clearly, $\frac{\Delta\psi_0}{\Delta\zeta}$ is not a flux function, and varies with θ on a given flux surface. So, the mean shearing rate varies with θ on a flux surface, such that the shearing rates are *not* symmetric at the inboard and the outboard mid-planes. In-out asymmetry of mean $E\times B$ shearing rate and fluctuations has been observed in DIII-D PT experiments [38]. The factor $\frac{R^2\psi'^2}{\mathcal{J}}$ captures the poloidal variation of the mean $E\times B$ shearing rate on a flux surface. To specify the flux surface shape, we use the local parametrized model for D shaped plasmas developed by Miller et *al* [34] and generalized for up-down asymmetric flux surfaces with finite squareness

$$R = R_0(r) + r\begin{cases}\cos(\theta + \sin^{-1}\delta_u(r)\sin\theta) & \forall\, 0 \leq \theta \leq \pi \\ \cos(\theta + \sin^{-1}\delta_l(r)\sin\theta) & \forall\, \pi \leq \theta \leq 2\pi\end{cases} \tag{4}$$

$$Z = \kappa(r) r \sin\left(\theta + \sigma\sin 2\theta\right). \tag{5}$$

Here, δ_u is upper triangularity, δ_l is lower triangularity, κ is ellipticity or elongation and σ is the squareness of the flux surface. For up-down symmetric flux surfaces, the shape is parametrized by a single triangularity parameter $\delta = \delta_u = \delta_l$. Note that r is the minor radius at $\theta = 0$. The primary advantage of this model as compared to a full numerical equilibrium is that the parameters can be individually varied. This allows for systematic studies of the effects of each parameter upon stability and transport for shaped flux surfaces. Here, we study the effects of each of these shaping parameters on the mean $E\times B$ shearing rate. The effects of triangularity recieves special focus. The magnetic field is defined in flux coordinates (ψ, θ, ζ) as:

$$\vec{B} = I\vec{\nabla}\zeta + \vec{\nabla}\zeta \times \vec{\nabla}\psi. \tag{6}$$

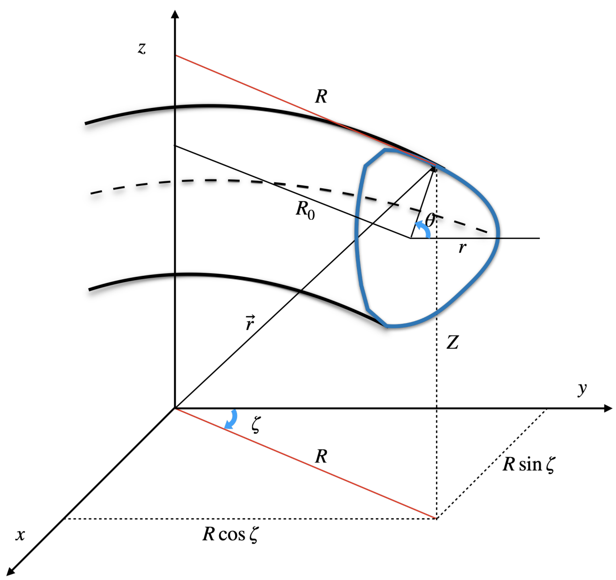

Figure 1. Coordinate conventions used for calculations.

The Jacobian $\mathcal{J}$ of transformation $\vec{r}(r,\theta,\zeta)$ is defined as $\mathcal{J} = \frac{\partial \vec{r}}{\partial r}\cdot\frac{\partial \vec{r}}{\partial \theta}\times\frac{\partial \vec{r}}{\partial \zeta} = \frac{1}{\vec{\nabla}r\cdot\vec{\nabla}\theta\times\vec{\nabla}\zeta}$. Since $\vec{r} = R\sin\zeta\hat{x} + R\cos\zeta\hat{y} + Z\hat{z}$, with R and Z given by equations(4) and (5), the Jacobian $\mathcal{J}$ becomes:

$$\mathcal{J} = R\left(\frac{\partial R}{\partial r}\frac{\partial Z}{\partial \theta} - \frac{\partial R}{\partial \theta}\frac{\partial Z}{\partial r}\right) \tag{7}$$

where

$$\frac{\partial R}{\partial r} = R_0' + \cos(\theta + \sin^{-1}\delta(r)\sin\theta) - S_\delta \sin(\theta + \sin^{-1}\delta(r)\sin\theta)\sin\theta$$

$$\frac{\partial R}{\partial \theta} = -r\sin(\theta + \sin^{-1}\delta(r)\sin\theta)\left(1 + \sin^{-1}\delta(r)\cos\theta\right)$$

$$\frac{\partial Z}{\partial r} = \kappa\left(1 + S_\kappa\right)\sin\left(\theta + \sigma\sin 2\theta\right) + \kappa\sigma S_\sigma \sin(2\theta)\cos\left(\theta + \sigma\sin 2\theta\right)$$

$$\frac{\partial Z}{\partial \theta} = \kappa r\cos\left(\theta + \sigma\sin 2\theta\right)\left(1 + 2\sigma\cos 2\theta\right)$$

where $\delta = \begin{cases} \delta_u & \forall\, 0 \le \theta \le \pi \\ \delta_l & \forall\, \pi \le \theta \le 2\pi \end{cases}$, $R_0' = \frac{\partial R_0}{\partial r}$ is Shafranov shift gradient, $S_\kappa = \frac{r}{\kappa}\frac{\partial \kappa}{\partial r}$ is ellipticity gradient, $S_\delta = \frac{r\frac{\partial\delta}{\partial r}}{\sqrt{1-\delta^2}}$ is triangularity gradient, and $S_\sigma = \frac{r}{\sigma}\frac{\partial\sigma}{\partial r}$ is squareness gradient. Thus, the mean ExB shearing rate depends not only on local triangularity δ, ellipticity κ and squareness σ but also on their local radial gradients S_δ, S_κ, and S_σ through the Jacobian $\mathcal{J}$. Here we assume R_0', S_κ and S_δ and S_σ are independent parameters. For vanishing squareness $\sigma = 0$, the Jacobian takes the familiar form shown in Ref [24] i.e.,

$$\mathcal{J} = R\kappa r\left[R_0'\cos(\theta) + \cos(x\sin\theta) + \sin(\theta + x\sin\theta)\sin\theta\left\{S_\kappa - S_\delta\cos\theta + (1+S_\kappa)\,x\cos\theta\right\}\right],$$

where $x = \sin^{-1}\delta(r)$. In the following, *we examine how the poloidal structure of the mean shearing rate varies with the flux surface shaping parameters for fixed $\frac{\partial^2}{\partial\psi^2}\Phi_0(\psi)$ and fixed ratio of radial correlation length to poloidal correlation angle i.e., for fixed $\frac{\Delta r}{\Delta\theta}$.*

2.1. Variation of mean shearing rate with triangularity δ

Notice that the geometric modulation to the mean $E\times B$ shearing rate is manifested through the term $\frac{R^2\psi'^2}{\mathcal{J}}$, where the explicit formulas for R, ψ', and $\mathcal{J}$ are given by equations(4), (3) and (7) respectively. Hence, the variations of mean $E\times B$ shearing rate with shaping parameters are inferred based on the dependence of the factor $\frac{R^2\psi'^2}{\mathcal{J}}$ on shaping parameters. Variations of the poloidal distribution of shearing rate and the flux surface averaged shearing rate with triangularity $\delta = \delta_u = \delta_l$ for the up-down symmetric equilibria are shown in figure(2). This figure clearly shows that:

- The shearing rate is maximal at the outboard mid-plane for positive triangularity δ^+. But the shearing rate is maximal off the outboard mid-plane for negative triangularity δ^-. So for δ^-, the shearing effect is stronger for finite k_x modes than for $k_x = 0$ modes. Recall that $k_x = 0$ modes are the most dangerous modes, which balloon at $\theta = 0$ and cause maximum transport by short-circuiting the plasma radially.

- The peak shearing rate bifurcates at a critical triangularity δ_{crit}. This is because the Jacobian (or equivalently the local safety factor ν) is a nonlinear function of δ, which exhibits spontaneous symmetry breaking (i.e., the minimum of the Jacobian bifurcates) for $\delta < \delta_{crit}$. For $\delta < \delta_{crit}$, the minimum splits into two and locates symmetrically above and below the outboard mid-plane for up-down symmetric triangularities. The δ_{crit} can be obtained from the solution of equation $\left[\frac{\partial^2}{\partial\theta^2}\frac{R^2}{\mathcal{J}}\right]_{\theta=0} = 0$. Clearly, the critical triangularity δ_{crit} for the onset of bifurcation is a function of triangularity gradient S_δ, ellipticity gradient S_κ and the Shafranov shift gradient R_0', squareness σ and squareness gradient S_σ. The critical triangularity is $\delta_{crit} \lesssim 0$ for typical experimental parameters.
- Peak shears move toward the good curvature region and the shearing rate at the outboard mid-plane $\theta = 0$ decreases with increasing δ^-.
- The poloidal width of the shear distribution increases, so that the flux surface averaged shear for NT is slightly higher than that for PT. The shearing is weaker at the poloidal mid-plane for NT, at *equal* values of radial force balance $\frac{\partial^2}{\partial\psi^2}\Phi_0(\psi)$, while the fluctuations intensity balloon at $\theta = 0$. The mismatch in ballooning angle and maximum shear location *may reduce the shearing efficiency for NT.* This may contribute to the observed increase in the L-H power threshold. Also, the transition might be initiated off the mid-plane for NT, in contrast to PT shapes.

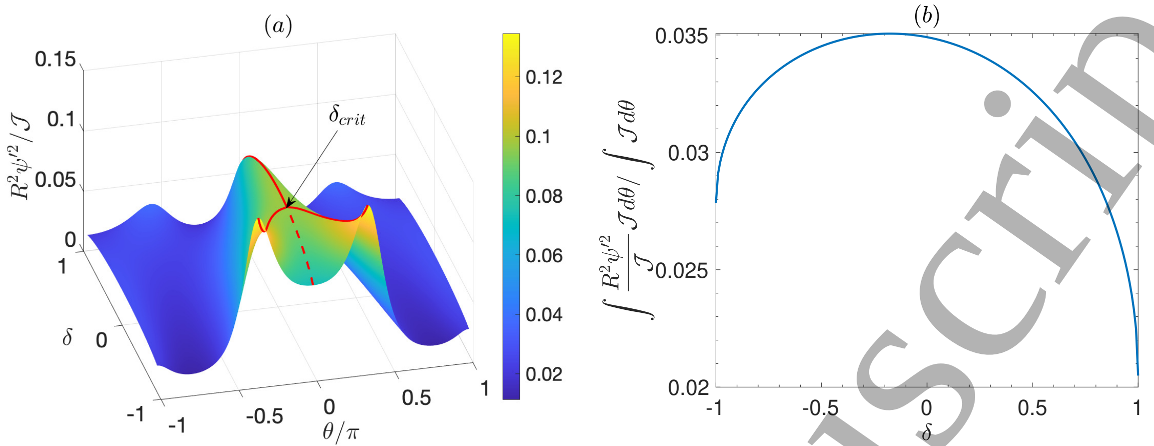

Figure 2. (a) Structure of mean ExB shearing rate in $(\theta-\delta)$ space. The solid red line tracks the maxima of the shearing rate and the dotted red line tracks the shearing rate at the mid-pane. Maximum shearing bifurcates at a critical δ. Here, $\delta_{crit} = -0.22$. Shearing at $\theta = 0$ is lower for δ^- than that for δ^+. (b) Flux surface averaged shearing rate is higher for δ^- than that for δ^+. Parameters: $R'_0 = -0.4$, $S_\delta = 0.8$, $\kappa = 1$, $S_\kappa = 1$, $\sigma = 0$, $S_\sigma = 0$, $\epsilon = 0.18$, $q = 3$.

2.1.1. Effect of up-down asymmetric triangularity The effect of flux surface up-down asymmetry due to up-down asymmetric triangularity is analyzed here. The plots in the figure(3) show how the poloidal structure of the mean shear and the flux surface averaged mean shear varies with the varying degree of asymmetry in upper and lower triangularities. These plots clearly show that:

- The flux surface averaged shearing rate is higher for negative upper triangularity δ_u^- than for positive upper triangularity δ_u^+, for fixed lower triangularity δ_l. Also for fixed upper triangularity δ_u, the shearing rate is higher for negative lower triangularity δ_l^- than that for positive lower triangularity δ_l^+. Flux surface averaged shearing decreases with $|\delta_l|$ because the flux gradient ψ' decreases with $|\delta_l|$.
- The poloidal distribution of shearing rate becomes asymmetric in θ when the upper and lower triangularities are different i.e., $\delta_u \neq \delta_l$. This is because the poloidal structure of the Jacobian above the mid-plane $(0 < \theta < \pi)$ depends on δ_u, whereas the poloidal structure of the Jacobian below the mid-plane $(\pi < \theta < 2\pi)$ depends

on δ_l. The structure of the shearing rate in $(\theta - \delta_u)$ space varies strongly with δ_l, as shown in figure(3). Notice the contrast with the up-down symmetric flux surface case shown in figure(2), where the max shearing rate (at $\theta = 0$) bifurcates into two equal strength peaks located symmetrically above and below the outer mid-plane. Comparison of the poloidal distribution of the shearing rate shows that the poloidal width is bigger for $\delta_u^-(\delta_l^-)$ than for $\delta_u^+(\delta_l^+)$, for fixed $\delta_l(\delta_u)$. Interestingly for strong $\delta_l^-(> 0.2)$, another peak of the shearing rate appears below the outboard mid-plane for all δ_u. The shearing peak below the outer mid-plane gets stronger and moves further away for the outboard mid-plane $(\theta = 0)$ on increasing δ_l^-. For $\delta_l > \delta_{l,crit}$ and $\delta_u > \delta_{u,crit}$ the shearing rate is maximal at the outboard mid-plane $(\theta = 0)$. For $\delta_l > \delta_{l,crit}$ and $\delta_u < \delta_{u,crit}$ the shearing rate is maximal above the outboard mid-plane $(\theta > 0)$. For $\delta_l < \delta_{l,crit}$ and $\delta_u > \delta_{u,crit}$ the shearing rate is maximal below the outboard mid-plane $(\theta < 0)$. For $\delta_l < \delta_{l,crit}$ and $\delta_u < \delta_{u,crit}$ the shearing rate peaks both at $\theta < 0$ and $\theta > 0$. Height and locations of the shearing peaks depends on values of δ_l, δ_u and how far they are from their respective critical values $\delta_{l,crit}$ and $\delta_{u,crit}$. Here, $\delta_{l,crit} = \delta_{u,crit} = \delta_{crit}$ since all other shaping parameters are up-down symmetric.

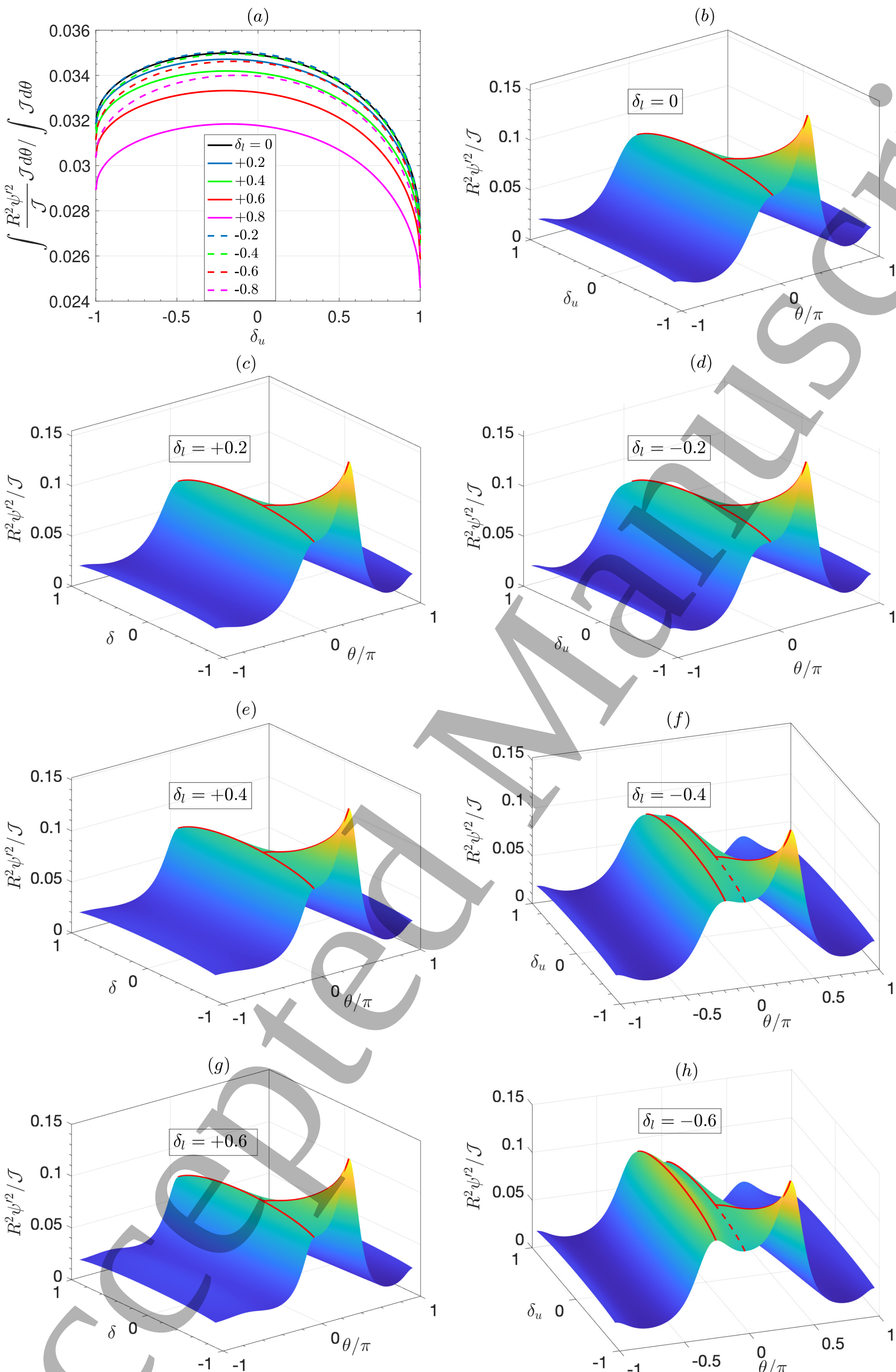

Figure 3. (a) Flux surface averaged shearing rate vs upper triangularity (δ_u) for various lower triangularities (δ_l) as parameters. (b-h) Structure of mean ExB shearing rate in ($\theta - \delta_u$) space for different δ_l's. The solid red line tracks the local maxima of the shearing rates at $\theta > 0$ and $\theta < 0$ and the dotted red line tracks the shearing rate at $\theta = 0$. For $\delta_u < \delta_{u,crit}$ and $\delta_l > \delta_u$ shearing rate is maximal above the outer mid-plane. For $\delta_l < \delta_{l,crit}$ and $\delta_u > \delta_l$ shearing rate is maximal below the outboard mid-plane. Other parameters same as in figure(2).

2.2. *Variation of mean shearing rate with triangularity gradient S_δ*

Variations of poloidal distribution of shearing rate with triangularity gradient S_δ are shown in figure(4). The figure clearly shows that

- Increasing S_δ moves the critical triangularity δ_{crit} for the onset of bifurcation towards increasing δ^-. That is, for higher S_δ the geometric bifurcation occurs at higher negative triangularity.
- The shearing rate at the outboard mid-plane decreases as S_δ increases.

This shows that the radial profile of the triangularity matters, not only its local value. The shearing rate increases significantly upon decreasing the triangularity gradient S_δ.

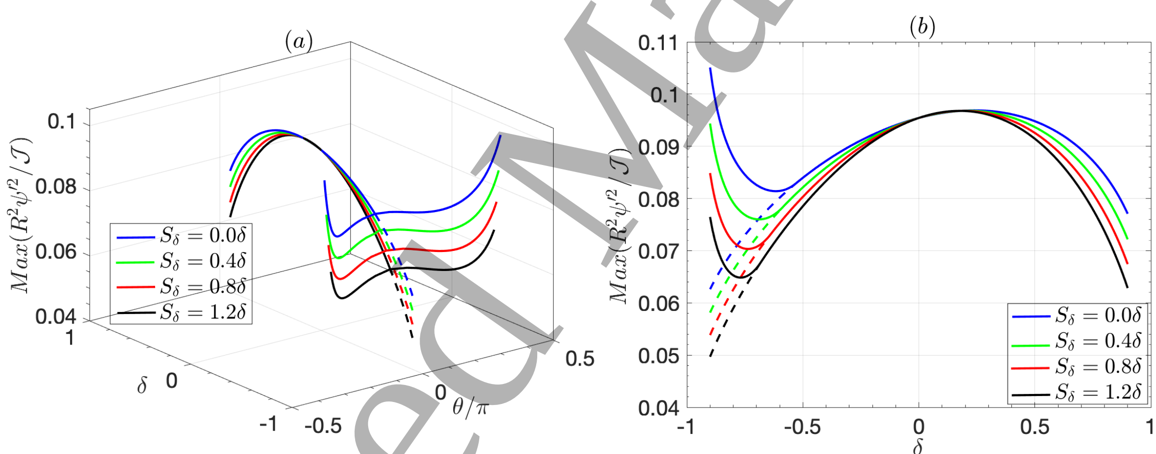

Figure 4. (a) Variations in $(\theta-\delta)$ structure of the max shearing rates (solid lines) and the shearing rate at $\theta=0$ (dashed lines) with triangularity gradient S_δ. The max shear bifurcation point δ_{crit} moves along δ^- on increasing S_δ. Shearing at $\theta=0$ decreases on increasing S_δ. (b) Projection of (a) on δ-axis. Other parameters same as in figure(2).

2.3. *Variation of mean shearing with Shafranov shift gradient R_0'*

Variations of the poloidal distribution of shearing rate with Shafranov shift gradient R_0' are shown in the plots in figure(5). The figure clearly shows that:

- The shearing rate increases with increasing $-R_0'$ for all δ. This is because of an increase in compression of flux surfaces, which occurs for increasing Shafranov shift.

This result is consistent with an earlier observation of Hahm et *al* [39] for circular flux surfaces.

- The critical triangularity δ_{crit} for bifurcation of the max shearing moves towards increasing δ^- for increasing $-R_0'$. That is, the geometric bifurcation occurs at stronger negative triangularities on increasing the Shafranov shift gradient.
- Since $R_0' \propto \frac{r}{R_0}\beta_p$ [40], this effect is significant for high-β_p(poloidal beta) ITB regimes. Negative triangularity experiments suggest that β_p for δ^- is higher than that for δ^+ [1]. Hence, the Shafranov shift induced boost of mean $E \times B$ shear is also important for NT discharges.

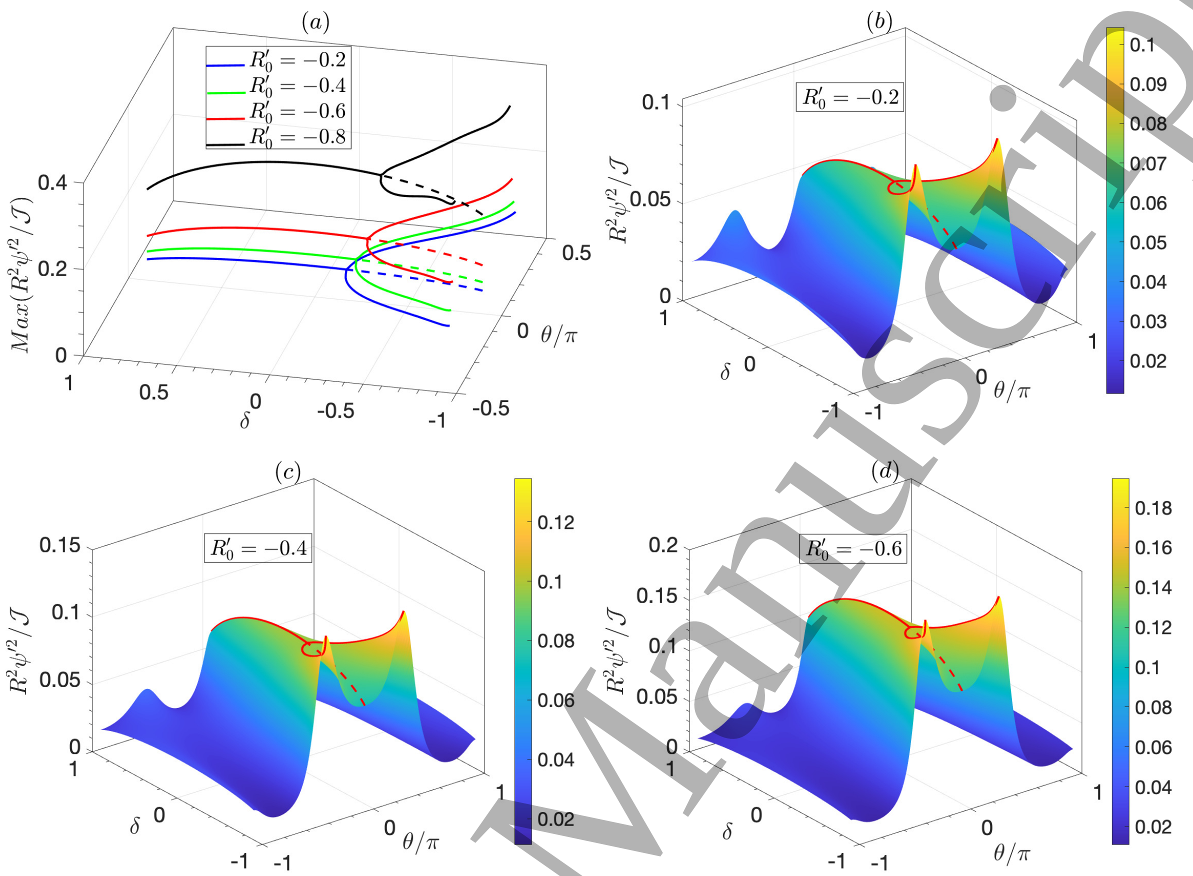

Figure 5. (a) Maximum shearing rates structure in $(\theta - \delta)$ space with Shafranov shift gradient R_0' as parameter. Shearing rate increases with $-R_0'$. The bifurcation point moves along increasing δ^- on increasing R_0'. Solid lines are the loci of maxima of the mean ExB shearing rate in $(\theta - \delta)$ space. The dashed lines track the shearing rate at $\theta = 0$. (b-d) 3d plots of shearing rates at different R_0'. Other parameters same as in figure(2).

Realistic MHD equilibrium study shows that R_0' is not a free parameter and varies with δ even for fixed β_p [41]. In fact, $-R_0'$ is higher for δ^- than for δ^+ for fixed β_p. As a result, mean shearing should increase when PT$\rightarrow$NT, even at fixed β_p, owing to enhanced Shafranov shift gradient. This in turn can improve confinement and increase β_p. The increase in β_p then drives stronger shearing and Shafranov shift, further increasing confinement and β_p. Thus, *enhanced mean $E \times B$ shearing by Shafranov shift produces positive feedback in the development of Shafranov shift induced transport bifurcation* [35–37]. Conversely, the Shafranov shift also has a positive effect on the feedback loop of mean $E \times B$ shear induced transport bifurcation, not only through a reduction of linear growth rate [42], but also through the enhanced $E \times B$ shearing rate.

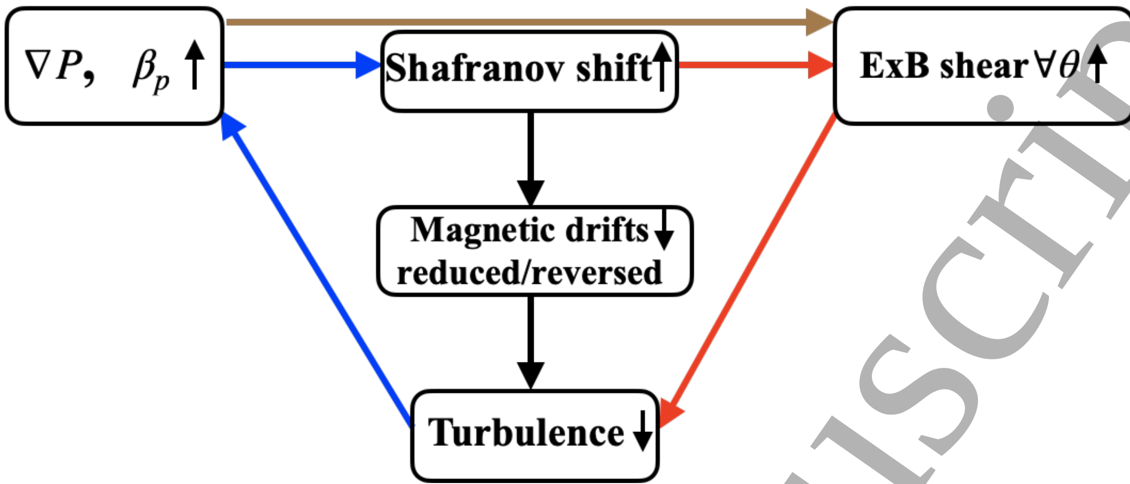

Figure 6. Feedback loops of mutual interactions of Shafranov Shift, mean ExB shear and turbulence. Shafranov shift and mean ExB shear reinforces each other.

Thus, Shafranov shift gradient affects turbulence in two distinct ways:

(i) The Shafranov shift stabilizes turbulence by reduction/reversal of magnetic drifts.

(ii) The Shafranov shift directly enhances the mean $E \times B$ shear, which causes additional turbulence suppression.

While (i) is well known [42, 43], (ii) is a *novel* finding in this paper. Both (i) and (ii) can cause bifurcation independently to enhance confinement, through their positive feedback loops. They can also work in tandem. This is shown in figure(6). However, (i) is often invoked as a mechanism of turbulence suppression and confinement improvement in high-β_p discharges [35–37], ignoring the role of mean $E \times B$ shear. But given the significant boost of mean ExB shear by Shafranov shift, the two mechanisms (i) and (ii) can reinforce each other to reduce the critical ∇P for onset of bifurcation to an internal transport barrier (ITB) state in PT reversed shear plasmas.

2.4. Variation of mean shearing with elongation κ and elongation gradient S_κ

Variations of poloidal distribution of shearing rate with elongation κ and elongation gradient S_k are shown in figure(7). The figure clearly shows that:

- the shearing rate increases with increasing κ and S_κ.
- The critical triangularity δ_{crit} for bifurcation of the maximum shearing is independent of κ, while the δ_{crit} moves towards higher δ^- upon an increase in S_κ.

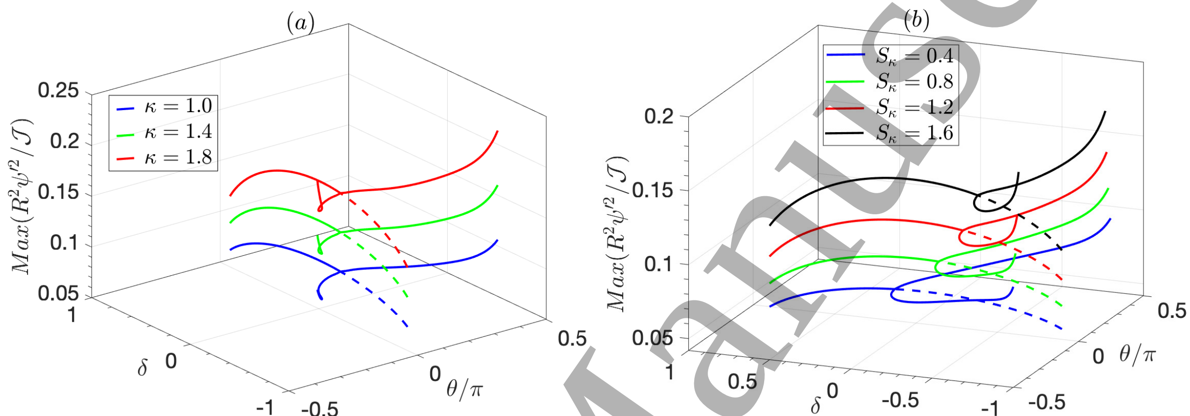

Figure 7. (a) Shearing rate elevates on increasing the elongation κ. (b) Shearing rate elevates and the bifurcation point moves along the δ^- direction on increasing the elongation gradient S_κ. Solid lines are the loci of maxima of the mean ExB shearing rate in $(\theta - \delta)$ space. The dashed lines track the shearing rate at $\theta = 0$. The solid red line tracks the maximum shearing rate and the dotted red line tracks the shearing rate at the mid-pane. Other fixed parameter : $R_0' = -0.4$, $S_\delta = 0.8$, $\kappa = 1$ for (b), $S_\kappa = 1$ for (a), $\sigma = 0$, $S_\sigma = 0$, $\epsilon = 0.18$, $q = 3$.

2.5. Variation of mean shearing with squareness σ and squareness gradient S_σ

Variations of poloidal distribution of shearing rate with squareness σ and squareness gradient S_σ are shown in figure(8). The calculations are done for up-down symmetric flux surface shapes i.e., $\delta = \delta_u = \delta_l$ to clearly delineate the effect of squareness σ. The figures clearly show that:

- The flux surface averaged shearing rate increases with increasing squareness and decreases with decreasing squareness, such that the shearing rate is higher for positive squareness σ^+ than that for negative squareness σ^-.
- However the shearing rate at $\theta = 0$ decreases with increasing σ such that the

shearing rate is higher for σ^- than that for σ^+.

- On increasing σ^+ the critical triangularity δ_{crit} for onset of geometric bifurcation increases i.e., moves towards higher δ^+. The maximal shearing peaks, located symmetrically about the outboard mid-plane, get stronger and the poloidal width of the shearing rate increases with increasing σ^+.
- On decreasing σ below zero, the geometric bifurcation of the maximal shearing rate in δ disappears. The shearing at $\theta = 0$ becomes the the maximal shearing and the poloidal width of the shearing distribution gets narrow on increasing σ^-.

Variations of shearing rate with squareness gradient S_σ are shown in figure(8). The figure clearly shows that the shearing rate increases with increasing S_σ, for all δ. However, the rate of increase of shearing with S_σ is weak. This is because the S_σ appears in multiple of σ in the Jacobian (see (7)) and since $|\sigma| < 1$, the effect of S_σ is weakened. Notice that the maximum shearing rate and the shearing rate at $\theta = 0$ increases with increasing S_σ. Also the critical triangularity δ_{crit} for the onset of geometric bifurcation moves towards increasing δ^-.

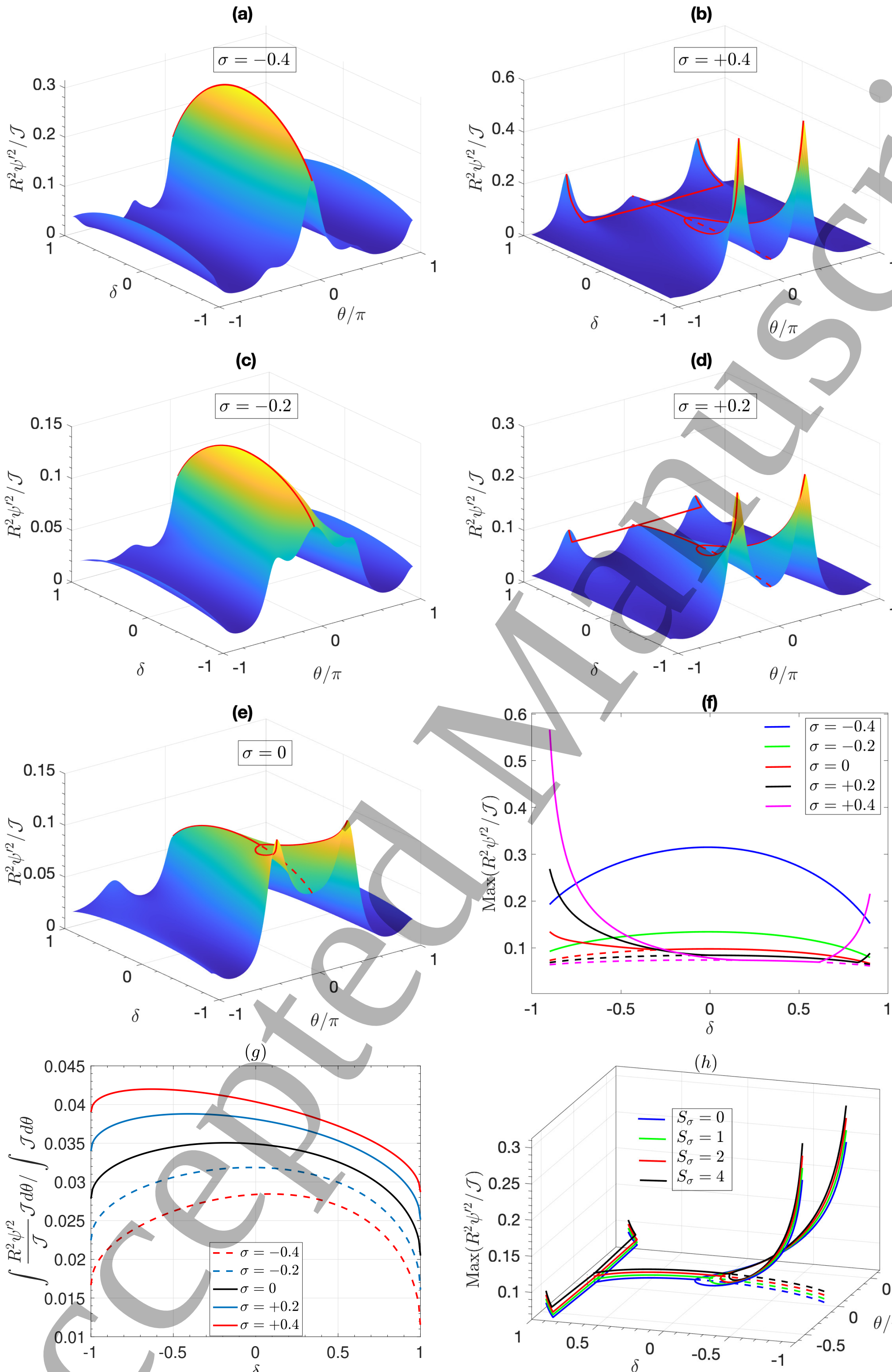

Figure 8. (a-e) Shearing rate variations in $(\theta - \delta)$ space for different squareness σ. (f) Maximum shearing rate variation with δ for different σ. The dashed lines in f) correspond to the shearing rates at $\theta = 0$, and the solid lines correspond to the max shearing rates. Notice that for $\sigma = -0.2, -0.4$ the max shearing rates are the shearing rates at $\theta = 0$. (g) Flux surface averaged shearing rate vs δ for different σ. (h) Shearing rate increases with squareness gradient S_σ. Other fixed parameters: $R_0' = -0.4$, $S_\delta = 0.8$, $\kappa = 1$, $S_\kappa = 1$, $S_\sigma = 0.4 sign(\sigma)$, $\epsilon = 0.18$, $q = 3$.

2.6. Variation of mean shearing with inverse aspect ratio ϵ and safety factor q

Variations of poloidal distribution of shearing rate with inverse aspect ratio ϵ and safety factor q are shown in figure(9). The figure clearly shows that:

- the shearing rate increases with increasing ϵ, while it decreases with incerasing q. This is because the flux gradient ψ'increases with increasing ϵ and decreases with increasing q.
- the critical triangularity δ_{crit} for bifurcation of the maximum shearing is independent of ϵ and q.

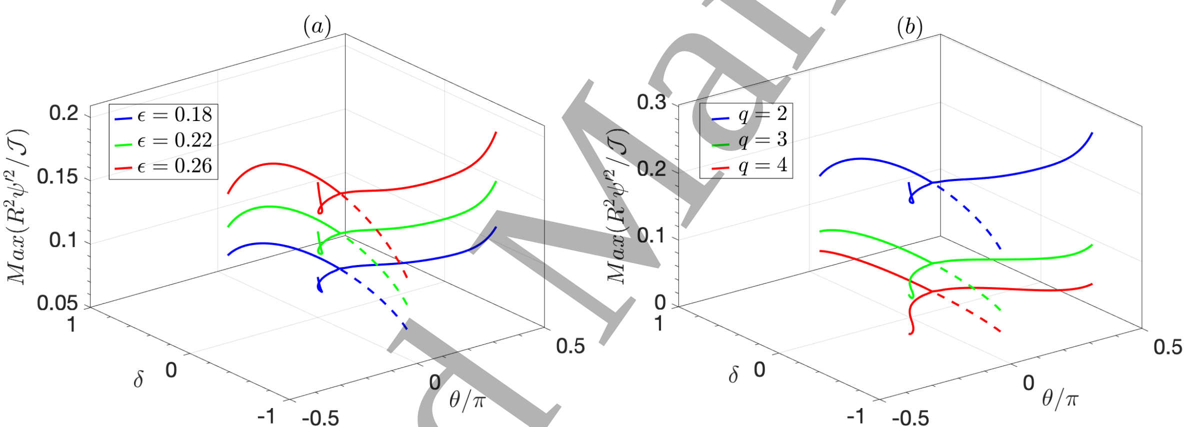

Figure 9. (a) Shearing rate elevates on increasing the inverse aspect ratio ϵ. (b) Shearing rate decreases on increasing the safety factor q. Solid lines are the loci of maxima of the mean ExB shearing rate in $(\theta - \delta)$ space. The dashed lines track the shearing rate at $\theta = 0$. Other fixed parameter : $R_0' = -0.4$, $S_\delta = 0.8$, $\kappa = 1$, $S_\kappa = 1$, $\sigma = 0$, $S_\sigma = 0$, $\epsilon = 0.18$ for (b), $q = 3$ for (a).

3. Discussion and conclusions

Mean $E\times B$ shear is well known to reduce turbulent transport and improve confinement, even in L-mode discharges [44]. Observation of improved confinement in the L-mode and diverging threshold power for L-H transition in strongly negative triangularity ($\delta < -0.18$) discharges has motivated this research to evaluate the mean $E \times B$ shear strength in matched positive and negative triangularity shapes. Here, we studied the flux surface shape dependent features of the mean $E\times B$ shearing rate, which are relevant to L-H transition physics in different plasma shapes. The Hahm and Burrell formula (1) for the mean $E \times B$ shearing rate [33] for an axisymmetric toroidal system is analyzed for negative and positive triangularity flux surface shapes, including the effects of up-down asymmetry, using the locally parametrized equilibrium model of Miller *et al* [34]. Here, the radial electric field shear $\frac{\partial^2}{\partial\psi^2}\Phi_0(\psi)$ is taken as fixed, and set by ion radial force balance. Detailed results are inferred from the dependence of the term $\frac{R^2\psi'^2}{\mathcal{J}}$ on the shaping parameters. The pre-factor $\frac{R^2\psi'^2}{\mathcal{J}}$ yields a purely geometrical modification to the mean $E \times B$ shearing rate. We study this factor as triangularity varies from $\delta > 0$ to $\delta < 0$. The results are summarized in the table(2). Notice that the shearing peaks symmetrically above and below the outboard mid-plane for up-down symmetric NT flux surface. This up-down symmetry of shearing is broken, and the shearing is strongest above the outboard mid-plane for up-down asymmetric NT shapes. Geometric modifications of the mean shearing can have following important implications.

- The Shafranov shift gradient directly boosts the shearing rate, for all δ. This is because of an increase in flux compression with increasing Shafranov shift gradient. This effect is significant for high-β_p regimes as well as NT discharges. This means that this effect will be even more important for NT high-β_p ITB regimes. Mean shear enhancement by Shafranov shift gradient provides additional turbulence suppression. This mechanism complements the commonly invoked mechanism for confinement improvement in high-β_p regimes, which is based on stabilization due to curvature drift reduction/reversal by Shafranov shift.

- Shearing is weaker at the outboard mid-plane for NT, at *equal* values of radial force balance $\frac{\partial^2}{\partial\psi^2}\Phi_0(\psi)$, while fluctuations balloon at $\theta = 0$. Thus, shearing efficiency is reduced for NT. This may contribute to the increase of the L-H power threshold for

NT. This mechanism complements the one based on loss of 2nd stability of ideal MHD ballooning modes [9, 10].

However, notice that going from PT to NT edge produces two competing effects. The *direct* effect of going from PT to NT is reduction of mean $E \times B$ shear at the outboard mid-plane. The indirect effect of going from PT to NT is the global (in θ) boost of mean $E \times B$ shear by *self-consistently* increased Shafranov shift. The parameters in the Miller's model are *not* all free. Thus, MHD equilibrium codes should be used for a more accurate calculation of the mean $E \times B$ shearing rate variations with the shaping parameters.

Shaping parameters	Effects on mean $E \times B$ shear			
	θ- symmetry of ω_E	flux surface averaged shear $\overline{\omega}_E$	shear at $\theta = 0$, ω_{E0}	δ_{crit} for geometric bifurcation
Triangularity δ (up-down symmetric) [Figure(2)]	up-down symmetric, maximum at $\theta \neq 0$ for NT $\implies$ shearing more effective for $k_x \neq 0$ modes	increases with decreasing δ such that $\overline{\omega}_E(\delta^-) > \overline{\omega}_E(\delta^+)$	decreases with decreasing δ such that $\omega_{E0}(\delta^-) < \omega_{E0}(\delta^+)$	depends on other shaping parameters ($\delta_{crit} \lesssim 0$)
Triangularity $\delta_u \neq \delta_l$ (up-down asymmetric) [Figure(3)]	up-down asymmetric, maximum at $\theta > 0$ or $\theta < 0$ for NT dependig on δ_l, δ_u.	increases with decreasing $\delta_{l,u}$ such that $\overline{\omega}_E(\delta^-_{l,u}) > \overline{\omega}_E(\delta^+_{l,u})$	decreases with decreasing $\delta_{l,u}$ such that $\omega_{E0}(\delta^-_{l,u}) < \omega_{E0}(\delta^+_{l,u})$	depends on other shaping parameters ($\delta_{u,crit} \lesssim 0$)
Triangularity gradient S_δ [Figure (4)]		decreases with increasing $\lvert S_\delta \rvert$	decreases with increasing $\lvert S_\delta \rvert$	decreases (moves towards higher δ^-)
Shafranov shift gradient R_0' [Figure (5)]		increases with increasing $-R_0'$	increases with increasing $-R_0'$	decreases (moves towards higher δ^-)
Elongation κ [Figure(7)]		increases	increases	no effect
Elongation gradient S_κ [Figure(7)]		increases	increases	decreases (moves towards higher δ^-)
Squareness σ [Figure (8)]		increases with increasing σ such that $\overline{\omega}_E(\sigma^-) < \overline{\omega}_E(\sigma^+)$	decreases with increasing σ such that $\overline{\omega}_E(\sigma^-) > \overline{\omega}_E(\sigma^+)$	increases (moves towards higher δ^+)
Squareness gradient S_σ [Figure (8)]		increases weakly with increasing S_σ	increases weakly with increasing S_σ	decreases (moves towards higher δ^-)
Inverse aspect ratio ϵ [Figure (9)]		increases with increasing ϵ	increases with increasing ϵ	no effect
Safety factor q [Figure (9)]		decreases with increasing q	decreases with increasing q	no effect

Table 2. Summary of effects of shaping parameters on shearing rate.

Finally, we present some suggestions for the experimentalists.

- Since the mean shearing is maximal off the outboard mid-plane for $\delta < \delta_{crit}$(∼NT), the eddy tilting should be maximum off the outboard mid-plane. For up-down symmetric shapes, eddy tilting should maximize symmetrically above and below the outboard mid-plane. For up-down asymmetric flux surface shapes, eddy tilting should maximize above the outboard mid-plane for $\delta_u < \delta_{crit}$ and $\delta_l > \delta_u$. Eddy tilting should maximize below the outboard mid-plane for $\delta_l < \delta_{crit}$ and $\delta_u > \delta_l$. This can be directly visualized in experiments by gas puff imaging [45]. The poloidal distribution of the tilt angle of the joint pdf of the radial and poloidal velocity fluctuations should also exhibit symmetry/asymmetry about the outboard mid-plane, depending on the flux surface symmetry. This implies that the poloidal envelope of the Reynolds stress should also exhibit similar symmetry/asymmetry due to flux surface shaping effects.
- Re-assess the role of mean $E \times B$ shear in high-β_p reversed shear ITB discharges given that Shafranov shift boosts the mean $E \times B$ shear.

Acknowledgments

This research was supported by U.S. DOE under Award No. DE-FG02-04ER54738. We thank T. S. Hahm for carefully reading the manuscript and useful discussions. Also thanks to Gyungjin Choi and DIII-D Negative Triangularity Cabalists for useful discussions. A. O. Nelson acknowledges support by the U.S. DOE awards DE-SC0022270 and DE-SC0022272.

[1] Austin M E, Marinoni A, Walker M L, Brookman M W, deGrassie J S, Hyatt A W, McKee G R, Petty C C, Rhodes T L, Smith S P, Sung C, Thome K E and Turnbull A D 2019 *Phys. Rev. Lett.* **122**(11) 115001 URL `https://link.aps.org/doi/10.1103/PhysRevLett.122.115001`

[2] Marinoni A, Austin M E, Hyatt A W, Walker M L, Candy J, Chrystal C, Lasnier C J, McKee

G R, OdstrÄil T, Petty C C, Porkolab M, Rost J C, Sauter O, Smith S P, Staebler G M, Sung C, Thome K E, Turnbull A D and Zeng L 2019 *Physics of Plasmas* **26** 042515 (*Preprint* https://doi.org/10.1063/1.5091802) URL https://doi.org/10.1063/1.5091802

[3] Fontana M, Porte L, Coda S and and O S 2018 *Nuclear Fusion* **58** 024002 URL https://doi.org/10.1088/1741-4326/aa98f4

[4] Camenen Y, Pochelon A, Behn R, Bottino A, Bortolon A, Coda S, Karpushov A, Sauter O, Zhuang G and the TCV team 2007 *Nuclear Fusion* **47** 510–516 URL https://doi.org/10.1088/0029-5515/47/7/002

[5] Coda S, Merle A, Sauter O, Porte L, Bagnato F, Boedo J, Bolzonella T, Février O, Labit B, Marinoni A, Pau A, Pigatto L, Sheikh U, Tsui C, Vallar M and Vu T 2022 *Plasma Physics and Controlled Fusion* **64** 014004 URL https://doi.org/10.1088/1361-6587/ac3fec

[6] Kikuchi M, Takizuka T, Medvedev S, Ando T, Chen D, Li J, Austin M, Sauter O, Villard L, Merle A, Fontana M, Kishimoto Y and Imadera K 2019 *Nuclear Fusion* **59** 056017 URL https://doi.org/10.1088/1741-4326/ab076d

[7] Paz-Soldan C 2021 *Plasma Physics and Controlled Fusion* **63** 083001 URL https://doi.org/10.1088/1361-6587/ac048b

[8] Han W, Offeddu N, Golfinopoulos T, Theiler C, Tsui C, Boedo J, Marmar E and the TCV Team 2021 *Nuclear Fusion* **61** 034003 URL https://doi.org/10.1088/1741-4326/abdb95

[9] Saarelma S, Austin M E, Knolker M, Marinoni A, Paz-Soldan C, Schmitz L and Snyder P B 2021 *Plasma Physics and Controlled Fusion* **63** 105006 URL https://doi.org/10.1088/1361-6587/ac1ea4

[10] Nelson A, Paz-Soldan C and Saarelma S 2022 *Nuclear Fusion* **62** 096020 URL https://dx.doi.org/10.1088/1741-4326/ac8064

[11] Merle A, Sauter O and Medvedev S Y 2017 *Plasma Physics and Controlled Fusion* **59** 104001 URL https://dx.doi.org/10.1088/1361-6587/aa7ac0

[12] Lao L, Ferron J, Miller R, Osborne T, Chan V, Groebner R, Jackson G, Haye R L, Strait E, Taylor T, Turnbull A, Doyle E, Lazarus E, Murakami M, McKee G, Rice B, Zhang C and Chen L 1999 *Nuclear Fusion* **39** 1785 URL https://dx.doi.org/10.1088/0029-5515/39/11Y/319

[13] Ferron J, Lao L, Luce T, Miller R, Osborne T, Rice B, Strait E and Taylor T 2000 *Nuclear Fusion* **40** 1411 URL https://dx.doi.org/10.1088/0029-5515/40/7/310

[14] Yu G, Li Z, Kramer G, Scotti F, Nelson A O, Diallo A, Lasnier C, Austin M E, Qin

X, Chen Y, Zheng Y, Zhu Y and Luhmann N C J 2023 *Physics of Plasmas* **30** ISSN 1070-664X 062505 (*Preprint* https://pubs.aip.org/aip/pop/article-pdf/doi/10.1063/5.0144711/17987372/062505_1_5.0144711.pdf) URL https://doi.org/10.1063/5.0144711

[15] Marinoni A, Brunner S, Camenen Y, Coda S, Graves J P, Lapillonne X, Pochelon A, Sauter O and Villard L 2009 *Plasma Physics and Controlled Fusion* **51** 055016 URL https://doi.org/10.1088/0741-3335/51/5/055016

[16] Merlo G, Huang Z, Marini C, Brunner S, Coda S, Hatch D, Jarema D, Jenko F, Sauter O and Villard L 2021 *Plasma Physics and Controlled Fusion* **63** 044001 URL https://doi.org/10.1088/1361-6587/abe39d

[17] Fontana M, Porte L, Coda S, Sauter O, Brunner S, Jayalekshmi A C, Fasoli A and and G M 2020 *Nuclear Fusion* **60** 016006 URL https://doi.org/10.1088/1741-4326/ab4d75

[18] Merlo G, Fontana M, Coda S, Hatch D, Janhunen S, Porte L and Jenko F 2019 *Physics of Plasmas* **26** 102302 (*Preprint* https://doi.org/10.1063/1.5115390) URL https://doi.org/10.1063/1.5115390

[19] Duff J M, Faber B J, Hegna C C, Pueschel M J and Terry P W 2022 *Physics of Plasmas* **29** 012303 (*Preprint* https://doi.org/10.1063/5.0065585) URL https://doi.org/10.1063/5.0065585

[20] Starr V P 1968 *Physics of negative viscosity phenomena* (McGraw-Hill)

[21] Diamond P H, S-I Itoh, Itoh K and Hahm T S 2005 *Plasma. Phys. Cont* **47** R35–R161

[22] Singh R and Diamond P H 2021 *Plasma Physics and Controlled Fusion* **63** 035015 URL https://doi.org/10.1088/1361-6587/abd618

[23] Biglari H, Diamond P H and Terry P W 1990 *Physics of Fluids B: Plasma Physics* **2** 1–4 (*Preprint* https://doi.org/10.1063/1.859529) URL https://doi.org/10.1063/1.859529

[24] Singh R and Diamond P 2022 *Nuclear Fusion* **62** 126073 URL https://dx.doi.org/10.1088/1741-4326/ac945e

[25] Kim E j and Diamond P H 2003 *Phys. Rev. Lett.* **90**(18) 185006 URL https://link.aps.org/doi/10.1103/PhysRevLett.90.185006

[26] Wagner F, Becker G, Behringer K, Campbell D, Eberhagen A, Engelhardt W, Fussmann G, Gehre O, Gernhardt J, Gierke G v, Haas G, Huang M, Karger F, Keilhacker M, Klüber O, Kornherr M, Lackner K, Lisitano G, Lister G G, Mayer H M, Meisel D, Müller E R, Murmann H, Niedermeyer H, Poschenrieder W, Rapp H, Röhr H, Schneider F, Siller G, Speth E, Stäbler

A, Steuer K H, Venus G, Vollmer O and Yü Z 1982 *Phys. Rev. Lett.* **49**(19) 1408–1412 URL https://link.aps.org/doi/10.1103/PhysRevLett.49.1408

[27] Wagner F 2007 *Plasma Physics and Controlled Fusion* **49** B1–B33 URL https://doi.org/10.1088/0741-3335/49/12b/s01

[28] Hinton F L 1991 *Physics of Fluids B: Plasma Physics* **3** 696–704 (*Preprint* https://doi.org/10.1063/1.859866) URL https://doi.org/10.1063/1.859866

[29] Hinton F L and Staebler G M 1993 *Phys. Fluids B* **5** 1281–1288

[30] Tala T J J, Heikkinen J A, Parail V V, Baranov Y F and Karttunen S J 2001 *Plasma Physics and Controlled Fusion* **43** 507 URL https://dx.doi.org/10.1088/0741-3335/43/4/309

[31] Ida K and Fujita T 2018 *Plasma Physics and Controlled Fusion* **60** 033001 URL https://dx.doi.org/10.1088/1361-6587/aa9b03

[32] Imadera K and Kishimoto Y 2022 *Plasma Physics and Controlled Fusion* **65** 024003 URL https://dx.doi.org/10.1088/1361-6587/aca9f9

[33] Hahm T S and Burrell K H 1995 *Physics of Plasmas* **2** 1648–1651 (*Preprint* https://doi.org/10.1063/1.871313) URL https://doi.org/10.1063/1.871313

[34] Miller R L, Chu M S, Greene J M, Lin-Liu Y R and Waltz R E 1998 *Physics of Plasmas* **5** 973–978 (*Preprint* https://doi.org/10.1063/1.872666) URL https://doi.org/10.1063/1.872666

[35] Ding S, Garofalo A M, Qian J, Cui L, McClenaghan J T, Pan C, Chen J, Zhai X, McKee G, Ren Q, Gong X, Holcomb C T, Guo W, Lao L, Ferron J, Hyatt A, Staebler G, Solomon W, Du H, Zang Q, Huang J and Wan B 2017 *Physics of Plasmas* **24** 056114 (*Preprint* https://doi.org/10.1063/1.4982058) URL https://doi.org/10.1063/1.4982058

[36] McClenaghan J, Garofalo A, Staebler G, Ding S, Gong X, Qian J and Huang J 2019 *Nuclear Fusion* **59** 124002 URL https://dx.doi.org/10.1088/1741-4326/ab4086

[37] Staebler G M, Garofalo A M, Pan C, McClenaghan J, Van Zeeland M A and Lao L L 2018 *Physics of Plasmas* **25** 056113 (*Preprint* https://doi.org/10.1063/1.5019282) URL https://doi.org/10.1063/1.5019282

[38] Rettig C L, Burrell K H, Stallard B W, McKee G R, Staebler G M, Rhodes T L, Greenfield C M and Peebles W A 1998 *Physics of Plasmas* **5** 1727–1735 (*Preprint* https://doi.org/10.1063/1.872841) URL https://doi.org/10.1063/1.872841

[39] Hahm T S, Artun M, Beer M A, Hammett G W, Lee W W, Li X, Lin Z, Mynick H E, Parker S E, Rewoldt G and Tang W M URL https://www.osti.gov/biblio/531073

[40] Lao L L, Hirshman S P and Wieland R M 1981 *The Physics of Fluids* **24** 1431–1440 (*Preprint* https://aip.scitation.org/doi/pdf/10.1063/1.863562) URL https://aip.scitation.org/doi/abs/10.1063/1.863562

[41] Song J, Paz-Soldan C and Lee J 2021 *Nuclear Fusion* **61** 096033 URL https://dx.doi.org/10.1088/1741-4326/ac189a

[42] Beer M A, Hammett G W, Rewoldt G, Synakowski E J, Zarnstorff M C and Dorland W 1997 *Physics of Plasmas* **4** 1792–1799 (*Preprint* https://doi.org/10.1063/1.872279) URL https://doi.org/10.1063/1.872279

[43] Bourdelle C, Hoang G, Litaudon X, Roach C and Tala T 2005 *Nuclear Fusion* **45** 110 URL https://dx.doi.org/10.1088/0029-5515/45/2/005

[44] Ritz C P, Lin H, Rhodes T L and Wootton A J 1990 *Phys. Rev. Lett.* **65**(20) 2543–2546 URL https://link.aps.org/doi/10.1103/PhysRevLett.65.2543

[45] Shesterikov I, Xu Y, Hidalgo C, Berte M, Dumortier P, Schoor M V, Vergote M, Oost G V and the TEXTOR Team 2012 *Nuclear Fusion* **52** 042004 URL https://dx.doi.org/10.1088/0029-5515/52/4/042004